



# Synthesis of nanostructured titania/zirconia membrane and investigation of its physical separation and photocatalytic properties in treatment of textile industries wastewater

Ayoub Taavoni-Gilan<sup>1</sup> · Ehsan Taheri-Nassaj<sup>2</sup> · Mojtaba Shamsipur<sup>3</sup>

Received: 12 February 2018 / Accepted: 30 July 2018 / Published online: 6 August 2018  
© Iranian Chemical Society 2018

## Abstract

Nanostructured TiO<sub>2</sub>/ZrO<sub>2</sub> composite membranes with varying compositions were obtained by sol–gel technique. The influence of 0–30 mol% zirconia doping on microstructure, water permeability, photocatalytic and physical separation properties, removal of methyl violet of textile industries wastewater and thermal and mechanical stability of titania/zirconia composite membranes was described. Firstly, alumina supports were coated with TiO<sub>2</sub> intermediate layers using the colloidal sol–gel route. The TiO<sub>2</sub>/ZrO<sub>2</sub> composite sols were prepared via a polymeric sol–gel method and dip-coated on TiO<sub>2</sub> intermediate layer. The samples were characterized by DLS, TG-DTA, XRD, FTIR, BET-BJH, UV–visible, SEM, TEM and AFM. It was shown that zirconia retards the phase transformation of anatase to rutile until at least 700 °C. The minimum pore size and maximum surface area obtained were 1.2 nm and 153 m<sup>2</sup>/g, respectively, attributed to the sample with 20 mol% zirconia. The mechanical strength of titania membranes was significantly improved by addition of zirconia. The most methyl violet removal efficiency obtained, with and without UV-irradiation, is 80.8 and 72.6%, respectively, attributed to the sample with 20 mol% zirconia.

**Keywords** Titania/zirconia membrane · Sol–gel method · Photocatalytic · Physical separation

## Introduction

Recently the development of efficient and environmentalist methods to wastewater treatment from water has become of fundamental importance, since pollution is increasing drastically. Recent advances in nanotechnology suggest that many of the issues involving water quality could be resolved or mostly improved using nanoparticles, nanofiltration or other products resulting from the development of nanotechnology [1, 2]. Ceramic membranes are currently being considered due to their potential applications in chemical,

petrochemical, pharmaceutical and food industries, where high pressure, high temperature and chemically harsh operation conditions are often faced. Recently, nanostructure titania membranes have received considerable attention because of their unique characteristics including semiconductance, high water flux, photocatalysis and chemical resistance compared to other membranes such as  $\gamma$ -alumina, silica and zirconia [3–5]. The potential applications of titania membranes include ultrafiltration processes and catalytic/photocatalytic membrane reactor systems for liquid and gas separations [6, 7]. The current limitation to practical application of titania-based membranes is due to the limited success that was met in producing crack-free layers, and the reduction of porosity and surface area by the sol–gel procedure which is the result of a partial kinetic anatase-to-rutile phase transformation occurring in titania upon calcination of the layer at temperatures of ~350 °C or higher. The phase transformation occurs by coalescence of small anatase particles into larger rutile grains, and is accompanied by notable grain and pore growth. However, a minimum calcination temperature of 450 °C is required to obtain well-defined, mechanically stable layers [8, 9]. Because of desirable application of the

✉ Ehsan Taheri-Nassaj  
taheri@modares.ac.ir

Ayoub Taavoni-Gilan  
a.taavoni@gmail.com

<sup>1</sup> Department of Materials Science and Engineering, Razi University, Kermanshah, Iran

<sup>2</sup> Department of Materials Science and Engineering, Tarbiat Modares University, P.O. Box 14115-143, Tehran, Iran

<sup>3</sup> Faculty of Chemistry, Razi University, Kermanshah, Iran

membrane at high temperature in many separation and/or reaction processes, thermal stability is also important. Being considered thermally stable at a specific temperature for a membrane means that its characteristics including mechanical strength, phase structure, especially the pore structure remain unchanged or have a negligible change at that temperature for a period of time analogous to practical applications [10]. However, the anatase-to-rutile phase transformation of pure titania occurs at about 350 °C [11]. On the other hand, the phase transformation from anatase (A) to rutile (R) will introduce a volume change of approximately 8%, which should be strictly avoided because it would induce film cracking in the formed membranes [12, 13]. There are two main approaches to avoid phase transformation [8]: (a) direct synthesis of rutile-phase titania, or (b) retarding phase transformation (and accompanying grain growth) to a temperature above the normal calcination temperature. Although the first approach can be a fast and effective way towards crack-free layer formation, the minimum grain size of the rutile phase is ~50 nm, which leads to the formation of a mesoporous membrane with ~20 nm pore size [14]. In other words, the anatase grain size, and therefore, pore size can be much smaller, which is desired for many applications. According to the second approach mentioned above, many dopants have been recognized that can inhibit the anatase–rutile phase transformation of titania [15–22]. The most widely used and efficient dopants are alumina and silica. Nevertheless, only a few authors mentioned one of the important disadvantages of these composite systems, which is the considerable decrease of chemical stability in harsh acidic or alkaline media [22]. Van Gestel et al. [19] illustrated that the alumina phase of a titania/alumina composite dissolved in harsh environments ( $\text{pH} \leq 3$  or  $\text{pH} \geq 11$ ), which led to a collapse of the pore structure. In this regard, zirconia has been found to be more appropriate due to its useful influence on both thermal and chemical stability [19–21]. To determine the required primary range of zirconia loading we used of zirconia–titania dual-phase diagram (considering the amount of solid solution).

The aim of this work is the preparation of  $\text{TiO}_2/\text{ZrO}_2$  composite membranes for removal of methyl violet (MV) of textile industries wastewater. Methyl violet is a family of organic compounds that are mainly used as dyes. Depending on the number of attached methyl groups, the color of the dye can be altered. Its main use is as a purple dye for textiles and to give deep violet colors in paint and ink. Methyl violet 10B is also known as crystal violet (and many other names) and has medical uses. In the present study zirconia doping is utilized to stabilize the anatase phase of titania membranes. The influence of doping on microstructure, thermal stability, photocatalytic, physical separation, as well as mechanical strength and water permeability in a wide interval of temperature is reported. We expect to obtain smaller pore

sizes in case of the composite membrane due to the mutual impediment of  $\text{ZrO}_2$  and  $\text{TiO}_2$  during phase transition and coarsening processes.

## Experimental

### Preparation of the polymeric sols and the composite membranes

Tetraethyl orthotitanate (98%, Aldrich) and zirconium(IV) *n*-propoxide (70%, Fluka), which are known as suitable precursors for the synthesis of  $\text{TiO}_2$  and  $\text{ZrO}_2$  nanostructure membranes, were applied as precursors. Moreover, nitric acid (65% solution, Merck) was applied as acid catalyst to promote the formation of polymeric sols. A given amount of a water (0.14 cc)/nitric acid (1 cc) solution was dissolved in a large volume of ethanol to keep the local concentration of water low. The resulting solution was added under vigorous stirring to a titanium tetraethoxide/ethanol solution after stirring for 15 min. Then it was stirred for 30 min and refluxed for 1 h producing a clear sol. Composite sols were obtained in one step by co-hydrolysis of zirconium(IV) *n*-propoxide and titanium tetra-ethoxide followed by peptization with  $\text{HNO}_3$ . In order to prevent infiltration, alumina supports were coated with  $\text{TiO}_2$  intermediate layers by applying the colloidal sol–gel method. Amounts of water, nitric acid, tetraethyl orthotitanate and zirconium(IV) *n*-propoxide used for preparing of colloidal sol were 0.75, 0.6, 1.75 and 10 cc, respectively. All samples were immersed in colloidal sol five times and each time for 30 s and obtained intermediated layer was dried at 80 °C for 3 h. The  $\text{TiO}_2/\text{ZrO}_2$  composite membranes were obtained by the polymeric sol–gel route. The composition of the top layer is already predefined during the preparation of the composite sol via using the corresponding quantities of the starting alkoxides (0–30 mol% Zr-alkoxide/70–100 mol% Ti-alkoxide). Titania/zirconia top layers were deposited by dip-coating technique (all samples were immersed in sol 5 times and each time for 30 s) on rutile titania-coated  $\alpha$ -alumina substrates [23, 24]. All experiments were performed in a dry nitrogen atmosphere to avoid possible reactions of the alkoxides with water vapor from ambient air. The layers were dried at 80 °C for 24 h and sintered with a heating rate of 10 °C/min in air to form the ceramic phase. The dried membranes were calcined in different temperatures for 3 h. Unsupported material was prepared through drying the sol in the air and subsequent calcinations under similar conditions as supported layers. No binders were used in order to avoid larger pores during the sintering process. Regarding the unsupported membranes, thermal treatment was performed in the temperature interval from gel to 800 °C. The coated samples were sintered at 500 °C for 3 h. In this paper, the pure titania and titania-(0,

5, 10, 20 and 30) mol% zirconia are denoted as TZ0 and TZ5, TZ10, TZ20 and TZ30, respectively (amount of tetraethyl orthotitanate used for all samples was 2.36 cc and amounts of zirconium(IV) *n*-propoxide were 0, 0.25, 0.5, 0.75 and 1 cc, respectively).

## Characterization methods

Particle size distribution of the prepared TZ0 and TZ20 polymeric sols was determined by dynamic light scattering technique (DLS, Malvern Instruments Ltd.). Crystallization behavior and phase transition of support and unsupported membranes were investigated by X-ray diffraction using a powder diffractometer (XRD, Philips) with Cu K $\alpha$  radiation. Thermal properties of the dried gels were characterized by thermogravimetry and differential thermal analysis (L60H1550 and STA 1460) in a nitrogen flow with a heating rate of 5 °C/min up to 900 °C. Fourier transform infrared spectroscopy (Bruker, ALPHA, Germany) was performed to investigate structural and specific molecule-groups information. The pore size distribution was determined from N<sub>2</sub> adsorption–desorption measurements (BEL Japan) using unsupported membranes. The specific surface area was calculated from the BET equation. The morphology, thickness and quality of the support and unsupported membranes were characterized by scanning electron microscopy (Phillips XL30) and transmission electron microscopy (TEM, EM 208, Philips) with an accelerating voltage of 30–100 kV, respectively. Surface morphology and topography of the prepared membranes was evaluated by atomic force microscopy (AFM, Dual Scope C-26, DME). The diffusive reflectance spectra (DRS) of the samples were recorded by a UV–visible spectrophotometer (Shimadzu, UV-2600) using BaSO<sub>4</sub> as a reference in the region from 250 to 750 nm. The water permeability, organic retention, MV removal efficiency and physical separation of membranes were measured with a dead-end home-fabricated membrane chamber according to Fig. 1. Pure water was pressurized with a nitrogen gas at transmembrane pressures (TMPs) from 0 to 8 kg/cm<sup>2</sup> and the permeate water flux were measured at room temperature using Eq. (1):

$$J = \Delta V / A \Delta t, \quad (1)$$

where  $V$  is the volume of permeate,  $A$  is the membrane active area and  $t$  is the filtration time. Instead of pure water, 200 mg/L of PEG (Fluka) solutions with different molecular weights were pressurized at a TMP of 2 kg/cm<sup>2</sup> to determine the molecular weight cut-off (MWCO) of the membranes and investigate their integrity. Organic carbon concentrations in the raw PEG solution and permeate water were measured using a total organic carbon (TOC) analyzer (Shimadzu, TOC-V CSH). MWCO curves were constructed by plotting the rejection of the individual oligomers in the

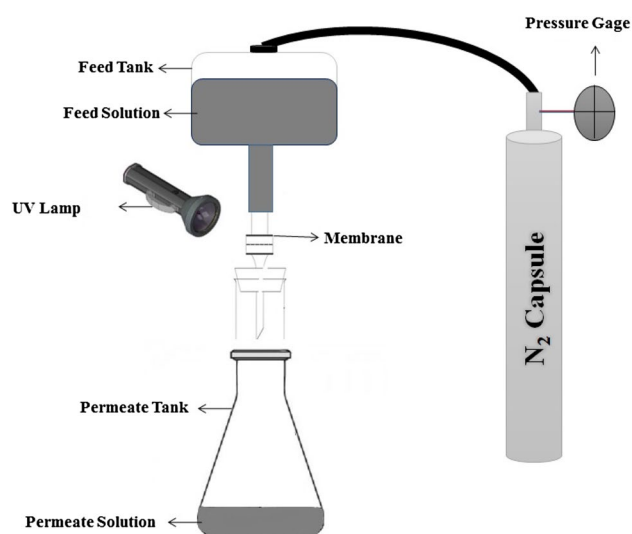


**Fig. 1** Schematic image of a photocatalytic membrane setup with a dead-end filtration cell used for filtration experiments

PEG mixtures against their molecular weight, with the membrane's MWCO determined as the MW that has a rejection of 90%. Solute rejection ( $R$ ) was calculated using Eq. (2):

$$\text{Rejection, } R(\%) = (1 - C_p / C_f) \times 100, \quad (2)$$

where  $C_p$  and  $C_f$  are the organic carbon concentration of permeate and feed, respectively. Also, the photocatalytic activity of the membranes was measured by the photo-degradation of MV aqueous solution. Initial pollutant concentration was set at 14 ppm and membranes in this solution were irradiated by a UV lamp. The MV removal efficiency was estimated by applying Eq. (2). The MV separation performance was investigated under 3 kg/cm<sup>2</sup> pressure [25].

## Results and discussion

### Unsupported membranes

#### Sol and particle size distribution

Particle size distribution of the prepared pure titania and titania/zirconia polymeric sols measured by DLS analysis is shown in Fig. 2. As seen, in low Zr dopant content (up to 20 mol%) the average particle size of sol increased with adding zirconia concentration. A further increase of zirconia concentration up to 30 mol% shows a decreasing trend which can be attributed to the much decrease in titanium percentage. This can be explained by the fact that the hydrolysis rate of tetraethyl orthotitanate is faster than zirconium(IV) *n*-propoxide and, therefore, fast tetraethyl orthotitanate hydrolysis causes bigger sol particles in comparison with

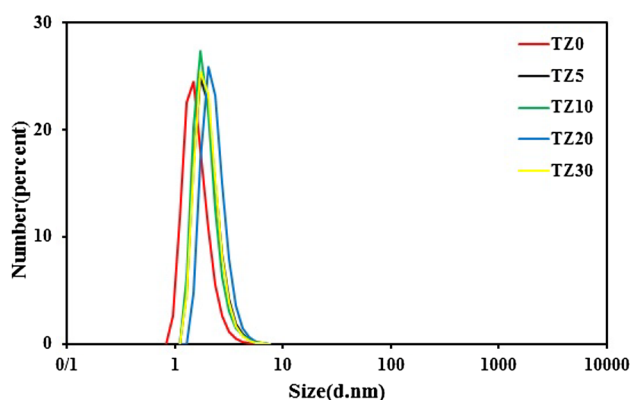


**Fig. 2** Changing particle size distribution of the polymeric sols with Zr doping

zirconium(IV) *n*-propoxide. It seems that addition of greater content of zirconium(IV) *n*-propoxide ( $\geq 20$  mol%) to titania sol decreases the particle size because of control hydrolysis rate [26].

SEM and TEM micrographs of the TZ0 and TZ20 unsupported membranes calcinated at 400 °C are shown in Fig. 3a–d. As revealed by SEM and TEM images, most of the particles are in the nanometer range and are spherical in shape and TZ20 samples consist of large particles that

are agglomerations of smaller particles in nanometer scale. Also, Fig. 3b, d shows that the particles tend to form more agglomerate together with adding zirconia which is due to the smaller particle size and increasing surface area. TEM figures (c and d) show the smaller particle size than SEM figures (a and b) which is due to the higher resolution of the TEM microscope and its ability to separate agglomerates.

### Surface area and pore structure characteristics

The effects of the amount of Zr doping on the pore structure of the TiO<sub>2</sub> samples are shown in Fig. 4a–c, respectively, and the surface area, pore size, pore volume and porosity data are summarized in Table 1. When the ZrO<sub>2</sub>/TiO<sub>2</sub> materials with a Zr content below 20 mol% were heated at 400 °C, the surface area increased to some extent compared to that of the undoped TiO<sub>2</sub> samples, and the pore size decreased. This may be attributed to the presence of a Zr compound and its suppression of grain growth. When the Zr content was below 20 mol%, the insufficient doping concentration of Zr induced slight changes in the microstructure. When the Zr concentration increased to 20 mol%, the doped Zr<sup>4+</sup> and ZrO<sub>2</sub> particles also contributed to the increase in the nonporous composition in the composite microstructure, resulting in the maximum specific surface area (153 m<sup>2</sup>/g) and the minimum pore size (1.2 nm). As the concentration increased

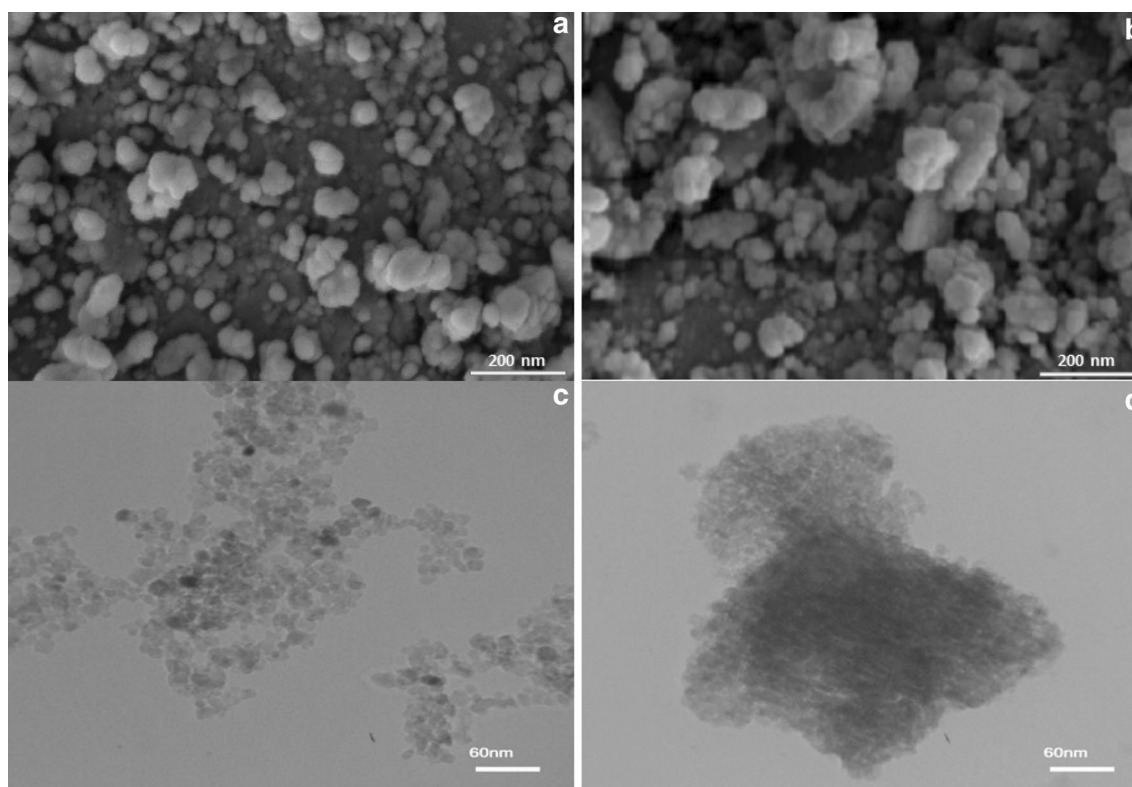


**Fig. 3** SEM (a, b) and TEM (c, d) diagrams of TZ0 and TZ20 samples calcinated at 500 °C, respectively

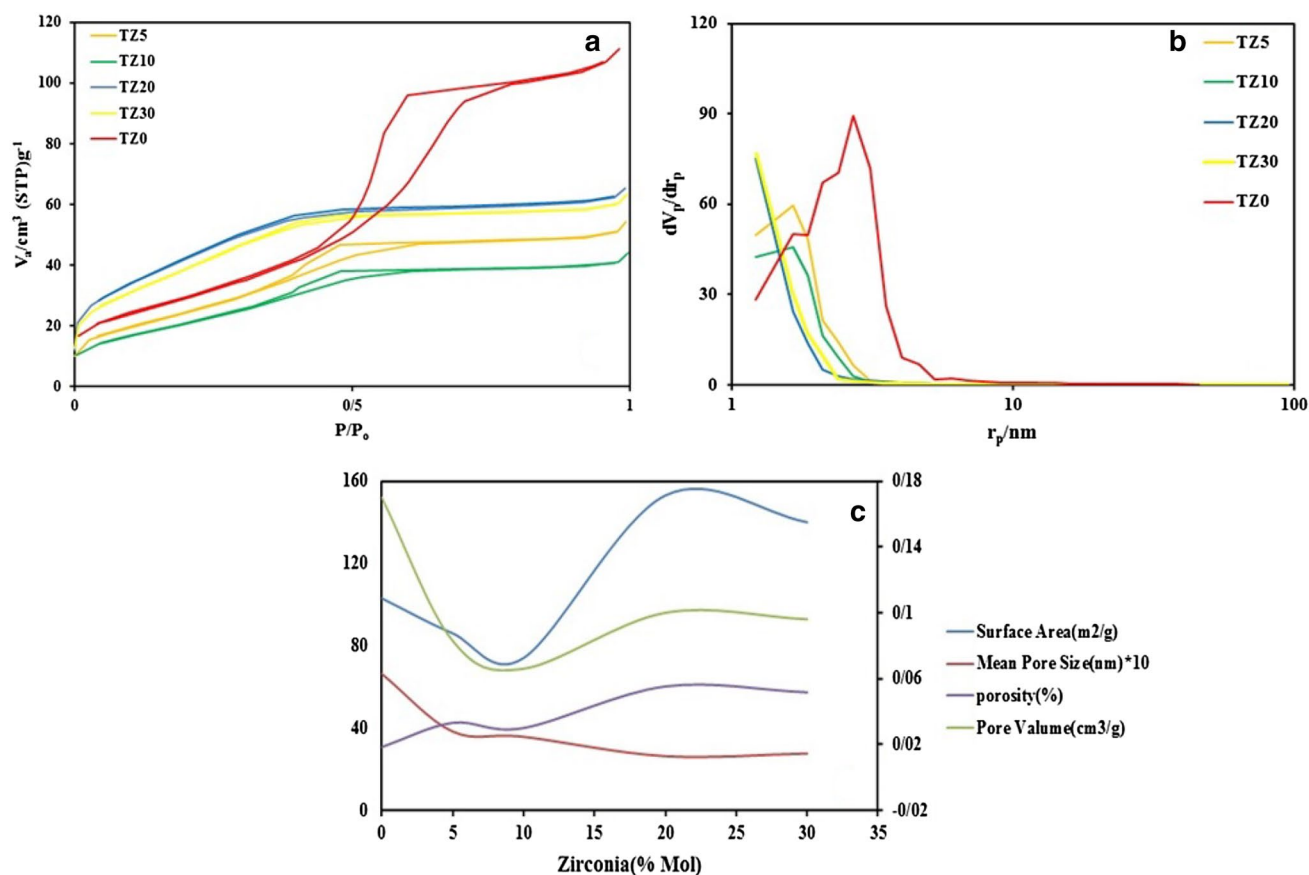


**Fig. 4** Effect of Zr doping concentration on **a** the adsorption–desorption isotherm, **b** pore size distribution of samples calcined at 500 °C and **c** comparison point chart

**Table 1** Average particle size in the sol, BET surface area, pore size and porosity of samples at 500 °C

Sample name	Particle size (nm)	BET surface area ( $\text{m}^2/\text{g}$ )	Pore size (nm)	Pore volume ( $\text{cm}^3/\text{g}$ )	Porosity (%)
TZ0	1.499	103	2.71	0.170	30/7
TZ5	1.736	86	1.64	0.083	42/5
TZ10	1.736	74	1.64	0.066	40.0
TZ20	2.010	153	1.21	0.100	60.2
TZ30	1.736	140	1.21	0.096	57.3

to 30 mol%, the specific surface area and pore size gradually decreased. This may be induced by the presence of a large quantity of Zr metal, based on the XRD data, which tended to exist in nonporous media and become a whole, leading to a decline in the specific surface area. The variation trend for the pore volume was similar to that for the pore size. Because a higher pore volume means a higher porosity, the Zr metal may tend to be part of the  $\text{TiO}_2$  sample and create large pores [13].

The physisorption isotherm of zirconia-doped titania was of type IV, similar as for pure titania, but the hysteresis loop changed from type H2 towards type H3 with increasing

zirconia concentration [27]. An H2 hysteresis loop is a property for a mesoporous material including spherical particles, with a relatively broad pore size distribution and a pore shape that is often explained as “ink bottle”-type. A change of the hysteresis loop shape towards H3 type describes that the mesopore size and shape changes, and an increased level of microporosity can be observed (see Fig. 4a). The main factors that can cause narrowing of the hysteresis loop are increased pore connectivity and/or decreased tortuosity [27, 28]. In terms percolation theory [28] the more highly connected the pore network is, the easier it becomes for vapor-filled pores to form a spanning cluster, and consequently the

hysteresis loop will become narrower. High tortuosity values are normally related to wide hysteresis loops provided that there is no substantial interference of capillary condensation metastability effects [29]. Also the point curve (Fig. 4c) confirms that TZ20 sample is the turning point of the diagrams and has a maximum surface area, pore volume and porosity and minimum pore size.

### Thermal stability and phase analysis

Figure 5a–c displays the XRD diagrams of the  $\text{TiO}_2\text{-ZrO}_2$  materials with different amounts of Zr doping ranging from 0 to 30 mol% and calcination temperatures ranging from 400 to 800 °C. The main peaks of anatase (101) at  $2\theta = 25.4^\circ$  were clearly shown at 400 °C in all samples (doped and undoped samples). For the undoped  $\text{TiO}_2$  samples, the main peaks of anatase (101) at  $2\theta = 25.4^\circ$  and rutile (110)

at  $2\theta = 27.5^\circ$  were obviously observed at 600 °C, while no diffractive peaks of the rutile displayed for the  $\text{TiO}_2\text{-ZrO}_2$  samples, which clearly exhibited the suppression effect of Zr doping on the  $A \rightarrow R$  phase transition. When the samples were further calcinated at 800 °C, a fingerprint peak for rutile emerged for the all samples, displaying an inadequate Zr concentration for rutile suppression. With the Zr doping amount increasing to 30 mol%, the anatase–rutile phase transition temperature was increased to 800 °C. The main peak of anatase for the TZ30 samples had a low intensity and wide width, indicating a small crystallite size as a result of Zr doping by limiting  $\text{TiO}_2$  crystal structure formation [13]. Observing from the size of ions  $\text{Zr}^{+}$  and  $\text{Ti}^{+}$ , the suppression of rutile phase is likely due to substitutional introduction of  $\text{Zr}^{+}$  into the  $\text{TiO}_2$  crystal lattice. The substitutional introduction has caused crystal deformation and also oxygen deficiency in order to achieve charge balance.

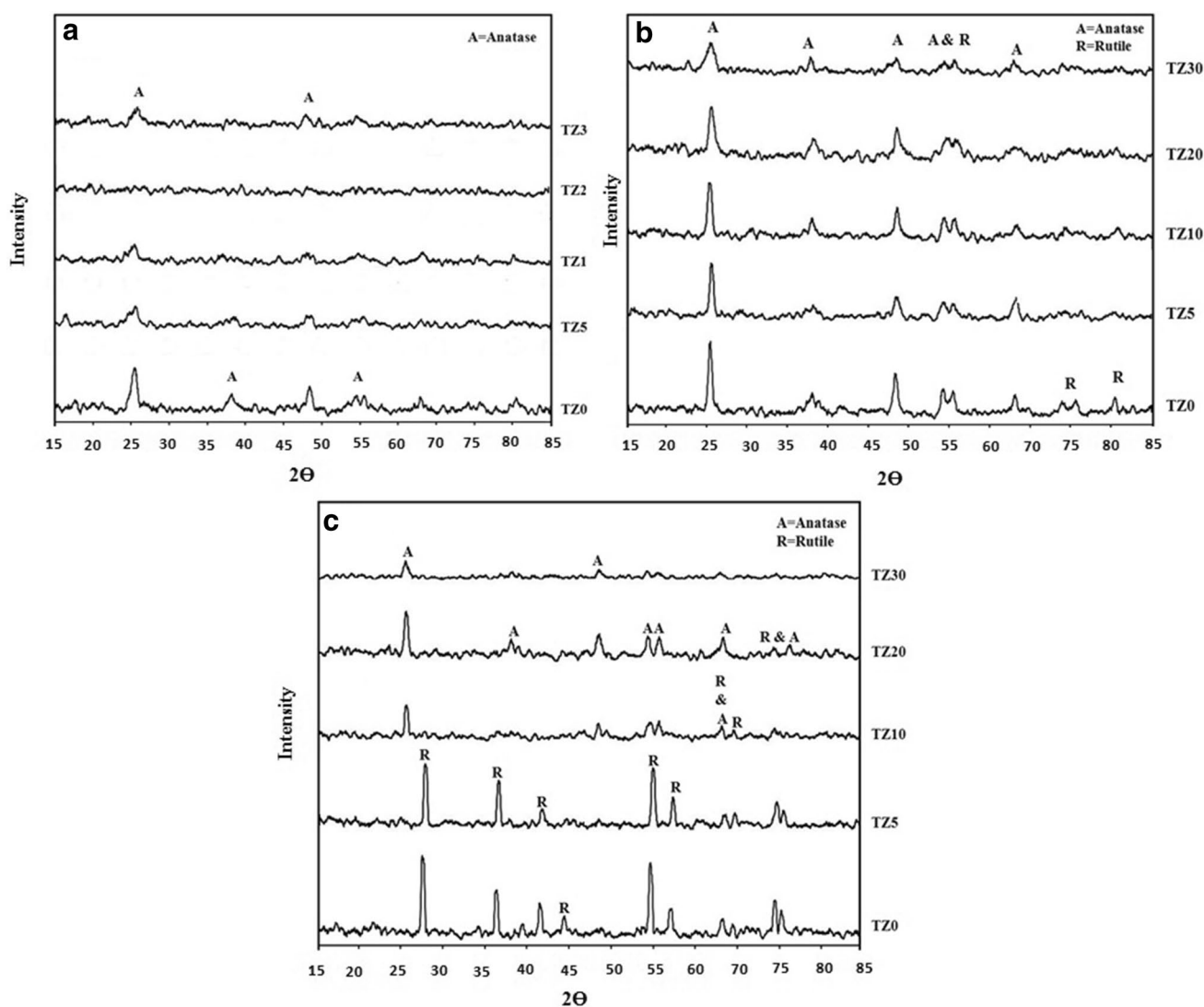


**Fig. 5** XRD patterns of the  $\text{ZrO}_2\text{-TiO}_2$  samples calcined at **a** 400 °C, **b** 600 °C and **c** 800 °C

The deformation in the lattice due to large amount of zirconium ion requires higher amount of deformation energy to be released, which causes the stabilization of anatase–rutile transformation. Crystalline zirconia was not observed. This may be explained by the observation of Yang et al. that the maximum solubility of zirconia in titania at 900 °C is about 7.5 mol% [10, 11]. However, our experiments were performed at temperatures of 400–800 °C, therefore the formation of a thermodynamically equilibrated solid solution is not ensured.

Figure 6a, b shows a typical TGA/DTA pattern of  $\text{TiO}_2$ – $\text{ZrO}_2$  samples with different amounts of Zr doping ranging from 0 to 30 mol% and calcination temperatures ranging from 0 to 900 °C. The TGA patterns (Fig. 6a) reveal weight losses occurring in two temperature intervals for all samples. A sharp weight loss occurred in the temperature interval 80–180 °C indicating the loss of water and solvent, followed by slower weight losses of organic substances in the interval 180–415 °C. The TGA patterns show that weight loss increased with doping of zirconia up to 20 mol% and then strongly decreased when Zr content increases to 30 mol%. The DTA curves shown in Fig. 6b contain information about water and solvent evaporation, structural changes and organic oxidation [30]. The first endothermic peak at ~100 °C in the DTA pattern corresponds to the removal of physisorbed water. A distinctive exothermic peak at ~142 °C may be attributed to the evaporation of ethoxy and propoxy groups in the form of ethanol and propanol. The heat effect is due to the heats of the hydrolysis and condensation reactions (minus the heat of evaporation of ethanol) that irreversibly occur when ethanol is removed from the polymers. Decomposition of organics and dehydroxylation happen between 200 and 400 °C. A sharp

exothermic peak at 237 °C corresponds to the amorphous-to-crystalline (anatase) phase transition. The exothermic peaks at 375–427 °C interval correspond to the anatase-to-rutile transformation. These results show that doping of zirconia retards anatase-to-rutile transformation that corresponds to XRD patterns (Fig. 5). The crystallization and anatase-to-rutile phase transition temperatures recorded by XRD are higher than that obtained by DTA. This can be ascribed to the fact that the temperature-programmed DTA experiment was performed with a heating rate of 5 °C/min, while faster heating in the XRD apparatus (10 °C/min) led to more sudden crystallization at a higher temperature.

## Supported membranes

### Mechanical stability and morphology of the membrane layer

Figures 7 and 8 present SEM and AFM micrographs of surface and cross section of the TZ0 and TZ20 membrane top layers. As shown in Figs. 7a and 8a, in the absence of zirconia, mechanically poor layers were formed. Cracking happened at TZ0 top layer upon deposition, drying and calcination at 500 °C for 3 h. Most probably the cracks were induced by capillary forces resulting from solvent that had penetrated from the titania sol into the underlying mesoporous layer and anatase-to-rutile transition. The figure clearly demonstrates that the crack propagates along large rutile grains that are embedded in the small-grained anatase microstructure. The mechanical strength at the same calcination temperature was discovered to be greatly improved by the addition of zirconia. A uniform, crack-free titania/zirconia layer on a colloidal titania $\alpha$ -alumina support is shown

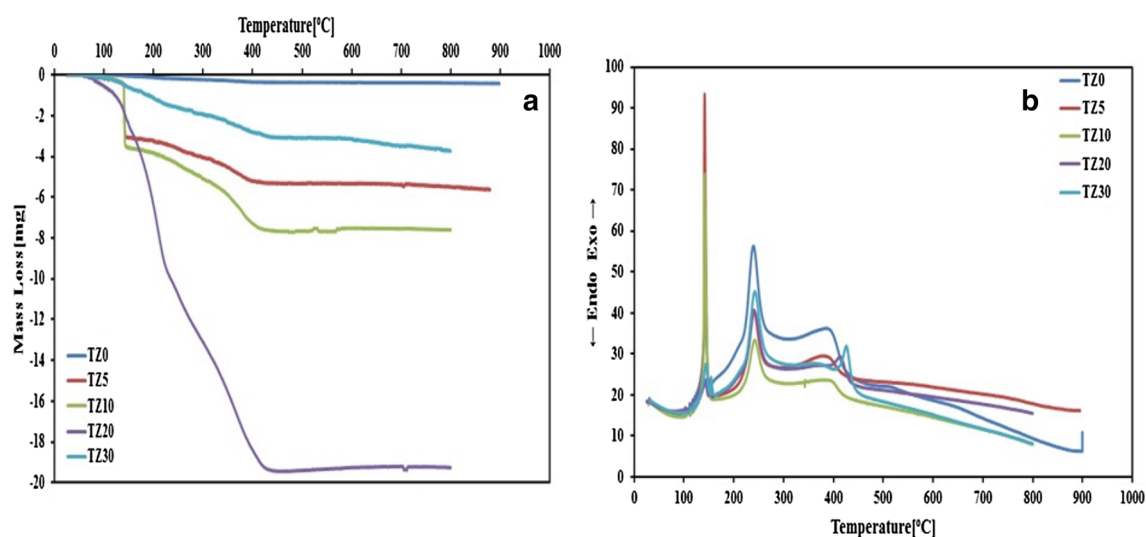
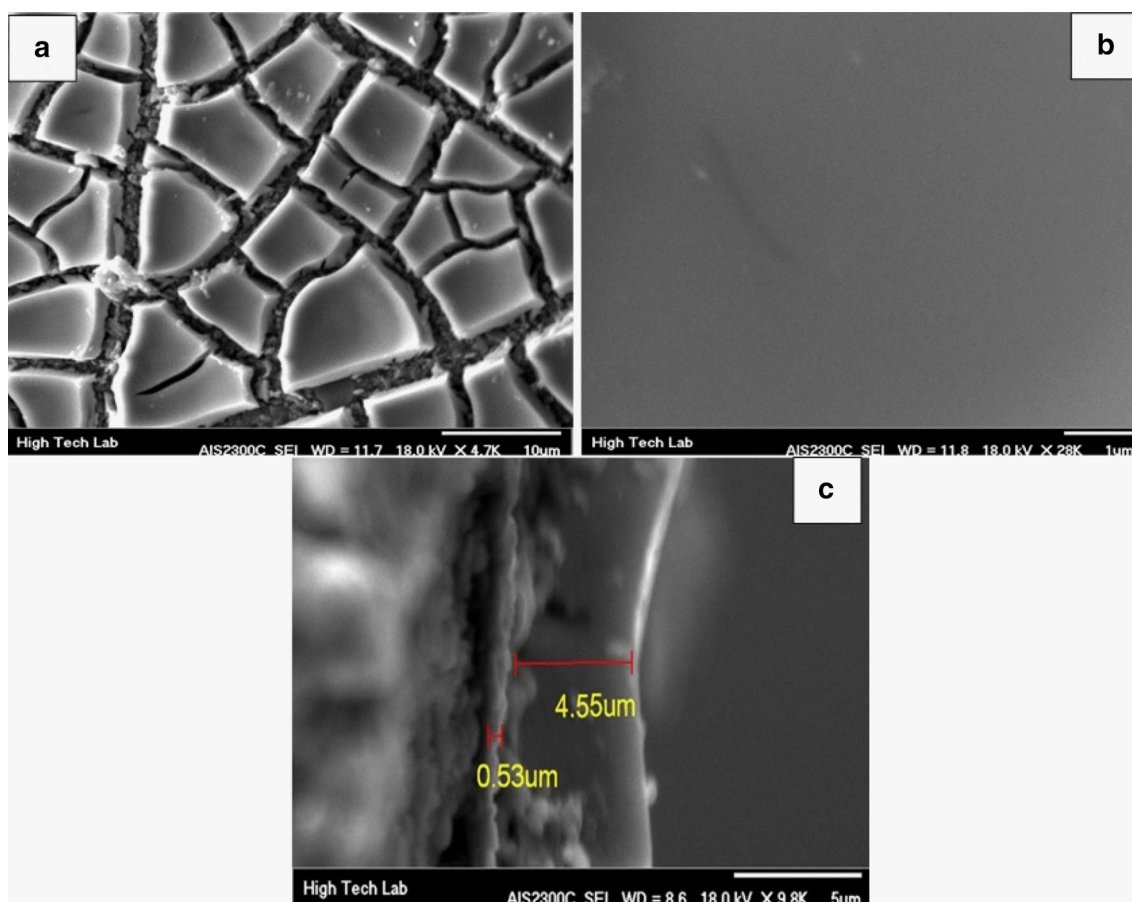


Fig. 6 a TG and b DTA curves of the dried polymeric gels



**Fig. 7** SEM micrographs of the surface of **a** TZO, **b** TZ20 and **c** cross section of the TZ20 samples calcined at 500 °C

in Figs. 7b and 8b. The average thickness of TZ20 layer (see Fig. 7c) is  $\sim 4.5 \mu\text{m}$ .

### Liquid permeability

Figure 9a, b shows water permeability and PEG retention of  $\alpha$ -alumina support,  $\alpha$ -alumina/rutile titania,  $\alpha$ -alumina/rutile titania/TZ0 and  $\alpha$ -alumina/rutile titania/TZ20 membranes at steady state. A relatively linear relationship between flux and pressure applied over the membrane exists, which indicates that the pressure difference is the only driving force for permeation (see Fig. 9a). Fluxes of 1–41 and 1–31  $\text{L m}^2/\text{h}$  were achieved in the pressure range of 0–6  $\text{kg}/\text{cm}^2$  for  $\alpha$ -alumina/rutile titania/TZ0 and  $\alpha$ -alumina/rutile titania/TZ20 membranes, respectively. The molecular weight cut-off (MWCO) calculated of retention curves (Fig. 9b) TZ0 and TZ20 membranes were 11,000 and 9000 Da, respectively. The MWCO of the TZ0 and TZ20 membranes, which are equal to a molecule diameter of approximately 3–4 nm and 2–3 nm, respectively, are relatively consistent with the pore size distribution of unsupported membranes (Fig. 4b) [31]. Apparently, the microstructural differences between materials with

different levels of zirconia doping do not have a considerable influence on liquid permeability PEG retention.

### Photocatalytic properties and separation performance

Separation performance of the nanostructured TZ0 and TZ membranes was determined by direct measurement of MV concentration in the permeate solution under 3  $\text{kg}/\text{cm}^2$  pressure. Concentration of feed MV solution was 13.60 ppm. MV absorbance curves of the feed and the permeate solutions are depicted in Fig. 10a. The concentration of permeate solutions/the MV removal efficiency [by using Eq. (2)] with TZ0, TZ5, TZ10, TZ20 and TZ30 membranes were determined to be 9.00 ppm/33.8%, 5.51 ppm/59.2%, 4.72 ppm/65.2%, 3.74 ppm/72.6% and 4.23 ppm/68.9%, respectively. The higher removal efficiency can be attributed to the smaller pores of the TZ composite membrane according to BET analysis according to the BET–BJH results in Fig. 4.

Photocatalytic activity of the pure titania and titania–zirconia membranes was determined by the absorbance change of MV feed solution under UV radiation after



**Fig. 8** AFM micrographs of the surface morphology of the **a** TZ0 and **b** TZ20 membranes calcined at 500 °C

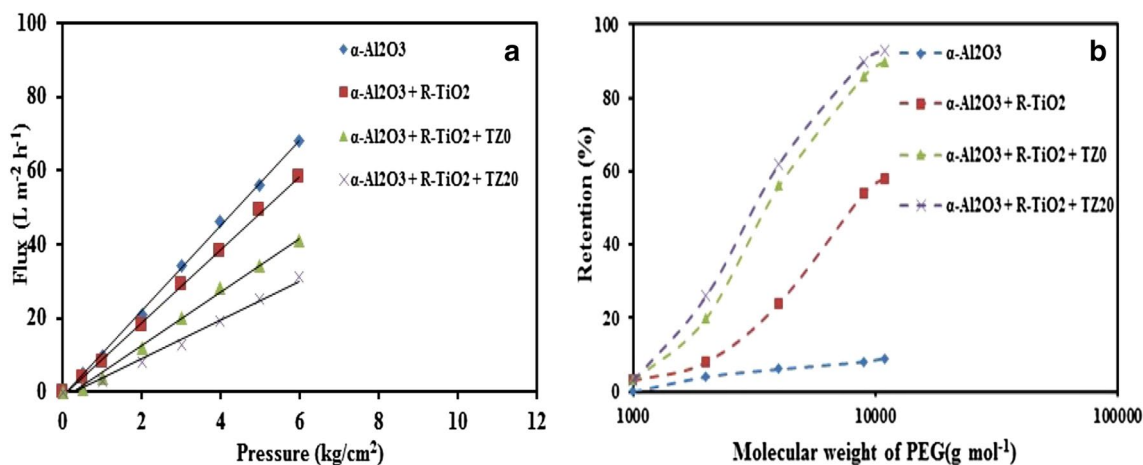
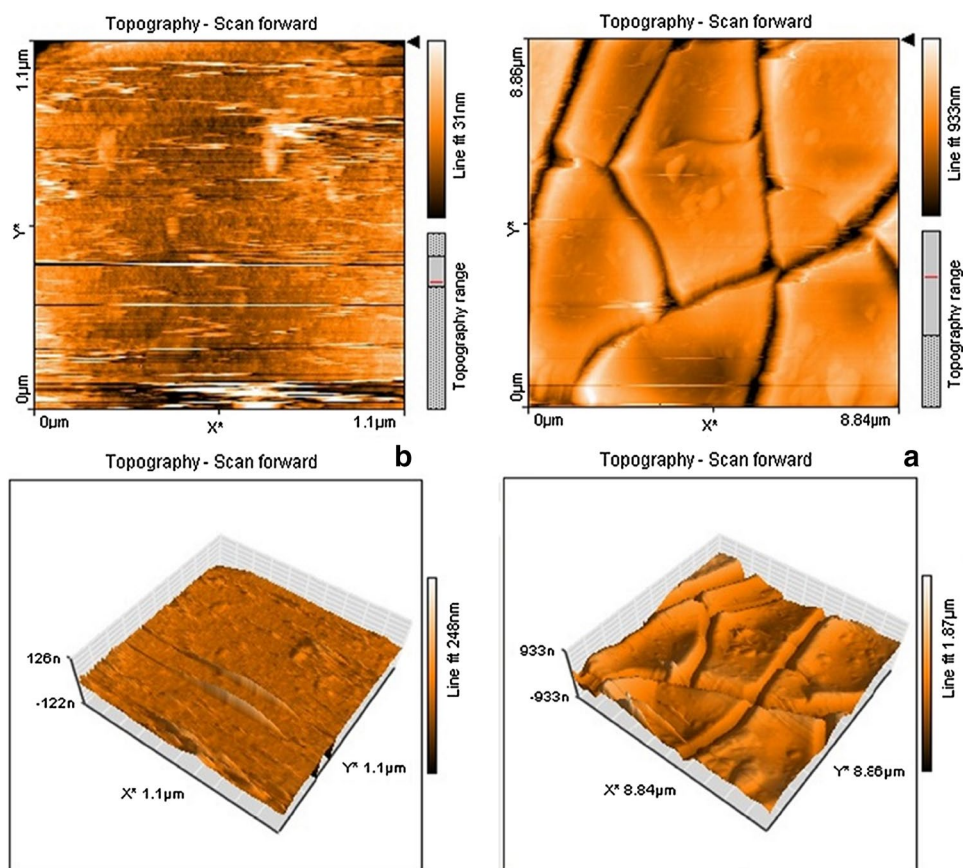


**Fig. 9** **a** Water permeability and **b** PEG retention of membranes

50 min as shown in Fig. 10b. The concentration of permeate solutions/the MV removal efficiency with TZ0, TZ5, TZ10, TZ20 and TZ30 membranes were determined to be 7.51 ppm/44.5%, 4.25 ppm/68.6%, 3.73 ppm/72.6%, 2.59 ppm/80.8% and 3.04 ppm/77.6%, respectively. It is well known that the photocatalytic activity of titania is essentially influenced by its crystal structure, grain size,

surface area and surface hydroxyl concentration [32, 33]. When zirconia is incorporated into titania membrane, both chemical and physical characteristics of the composite membrane maybe different from titania membrane. These changes have influence on the photocatalytic activity of the TZ composite membrane in comparison to TZ0 membrane. The results indicate that the photocatalytic activity

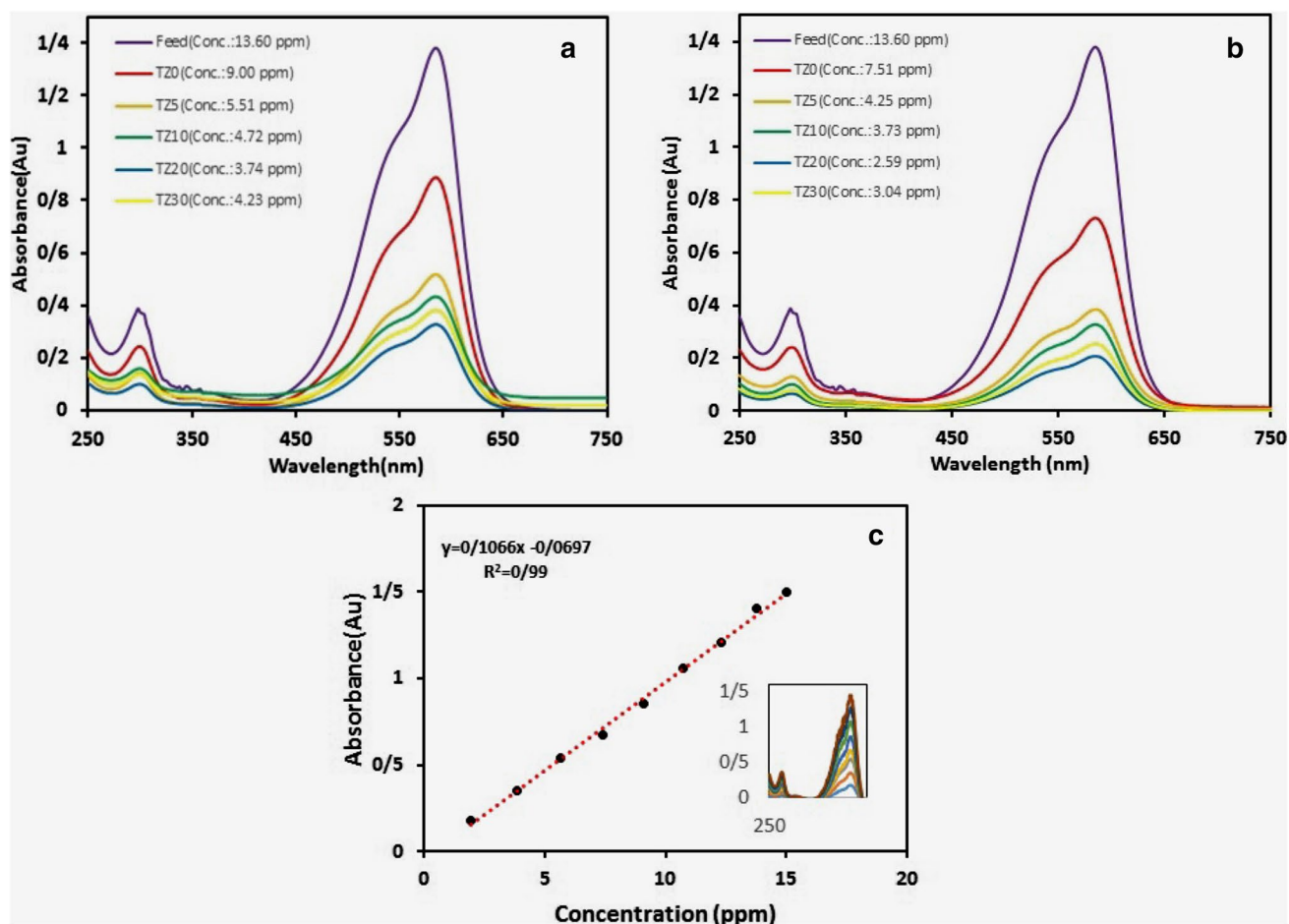


Fig. 10 Absorbance curves of MV solutions **a** before and **b** after UV-irradiation and **c** calibration curve of MV solutions in 584 nm wavelength

of the TZ membranes is more than that of the pure titania membrane. The increased photocatalytic activity can be related to the following issues. Firstly, the grain size of titania strongly decreases and specific surface area clearly increases, when zirconia is doped to the titania membrane. The decrease in the crystallite size probably results in a larger driving force for charge transfer existing in a quantum-sized titania in the mixed membrane. The increasing of surface area probably causes a higher adsorption toward organic contaminants. Also, the increase in surface hydroxyl content traps more holes in the valence band and thus prevents electron–hole recombination [34, 35] which is schematically represented in Fig. 11. These factors enhance the photocatalytic activity of titania–zirconia composite membranes. Therefore, though the TZ composite membrane contains a content of zirconia, the photocatalytic activity of the composite membrane is still higher than that of the TZ0 membrane. It can be concluded that a small concentration of zirconia in the TZ composite membrane plays an important role in increasing photocatalytic activity. Also, it seems that the higher roughness of the TZ

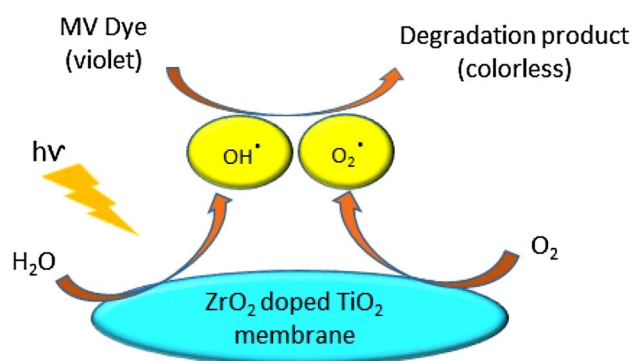


Fig. 11 Schematic of the photocatalytic degradation of methyl violet dye using  $\text{TiO}_2$ – $\text{ZrO}_2$  membrane

membrane (according to the AFM results in Fig. 8) allows a better ability to capture the incident photon energy since a larger surface extension facilitates the photo-degradation process. In fact, this surface not only enables the adsorption of a greater number of pollutant molecules, but also creates a rough environment that causes a multiple light

reflection and thus increases the amount of absorbed photons for photo-degradation process [36].

MV concentration in the solutions was evaluated using calibration curve of MV (absorbance values of MV in 584 nm wavelength) as shown in Fig. 10c.

## Conclusions

Nanostructured Zr-doped titania membranes have been synthesized via the polymeric sol–gel method. XRD diagrams and TEM images indicated that Zr doping inhibited TiO<sub>2</sub> grain coarsening and retarded the phase transformation of anatase to rutile until at least 700 °C. The minimum pore size and maximum surface area obtained are 1.2 nm and 153 m<sup>2</sup>/g, respectively, attributed to the sample with 20 mol% zirconia. The mechanical strength of titania membranes was significantly improved by addition of zirconia. The most methyl violet removal efficiency obtained, with and without UV-irradiation, is 80.8 and 72.6%, respectively, attributed to the sample with 20 mol% zirconia. Water permeability was decreased by zirconia doping.

## References

1. S. Filice, D. D'Angelo, S. Libertino, I. Nicotera, V. Kosma, V. Privitera, S. Scalse, *Carbon* **82**, 489 (2015)
2. V. Tajer-Kajinebaf, H. Sarpoolaky, T. Mohammadi, *Ceram. Int.* **40**, 1747 (2014)
3. C. Guizard, A. Julbe, A. Larbot, L. Cot, *Key Engineering Materials* (Trans Tech Publication, Zurich, 1992)
4. C.-H. Chang, R. Gopalan, Y. Lin, *J. Membr. Sci.* **91**, 27 (1994)
5. A. Karami, *J. Iran. Chem. Soc.* **7**, S154–S160 (2010)
6. T. Tsuru, D. Hironaka, T. Yoshioka, M. Asaeda, *Sep. Purif Technol.* **25**, 307 (2001)
7. A. Ahmad, M. Othman, H. Mukhtar, *Int. J. Hydrogen Energy* **29**, 817 (2004)
8. K.-N.P. Kumar, *Nanostructured Ceramic Membranes: Layer and Texture Formation* (Ph.D. Thesis, University of Twente, Enschede, The Netherlands, 1993), pp 113
9. Y.-S. Lin, C.-H. Chang, R. Gopalan, *Ind. Eng. Chem. Res.* **33**, 860 (1994)
10. J. Yang, J.M.F. Ferreira, *Mater. Res. Bull.* **33**, 389 (1998)
11. B. Kingery, H. Bowen, (Wiley, New York, 1976)
12. K. Okada, N. Yamamoto, Y. Kameshima, A. Yasumori, K.J. MacKenzie, *J. Am. Ceram. Soc.* **84**, 1591 (2001)
13. Y. Cai, X. Chen, Y. Wang, M. Qiu, Y. Fan, *Microporous Mesoporous Mater.* **201**, 202 (2015)
14. K.-N.P. Kumar, K. Keizer, A.J. Burggraaf, *J. Mater. Chem.* **3**, 917 (1993)
15. P. Sánchez-Soto, M. Aviles, G. Colón, M. Macias, J. Navio, *Mater. Lett.* **20**, 339 (1994)
16. J. Sekulic-Kuzmanovic, *Mesoporous and Microporous Titania Membranes* (University of Twente, Enschede, 2004)
17. R. Gopalan, Y. Lin, *Ind. Eng. Chem. Res.* **34**, 1189 (1995)
18. R. Arroyo, G. Cordoba, J. Padilla, V. Lara, *Mater. Lett.* **54**, 397 (2002)
19. C.V. Tim Van Gestel, A. Buekenhoudt, C. Dotremont, R.L. Jan Luyten, B. Van der Bruggen, G. Maes, *J. Membr. Sci.* **224**, 3 (2003)
20. D.-S. Bae, K.-S. Han, S.-H. Choi, *J. Mater. Sci. Lett.* **16**, 658 (1997)
21. D.-S. Bae, K.-S. Han, S.-H. Choi, *Ceram. Trans.* **81**, 349 (1997)
22. Y. Cai, Y. Wang, X. Chen, M. Qiu, Y. Fan, *J. Membr. Sci.* **476**, 432 (2015)
23. P.M. Biesheuvel, H. Verweij, *J. Membr. Sci.* **156**, 141 (1999)
24. A. Taavoni-Gilan, E. Taheri-Nassaj, M. Shamsipur, *Mater. Technol.* **32**, 1 (2016)
25. R. Rohani, M. Hyland, D. Patterson, *J. Membr. Sci.* **382**, 278 (2011)
26. A. Ismail, I. Ibrahim, M. Ahmed, R. Mohamed, H. El-Shall, *J. Photochem. Photobiol A* **163**, 445 (2004)
27. K.S. Sing, *Pure Appl. Chem.* **57**, 603 (1985)
28. G. Armatas, C. Salmas, M. Loulodi, G. Androustopoulos, P. Pomonis, *Langmuir* **19**, 3128 (2003)
29. J. Sekulić, A. Magraso, J.E. ten Elshof, D.H.A. Blank, *Microporous Mesoporous Mater.* **72**, 49 (2004)
30. J. Ragai, W. Lotfi, *Colloids Surf.* **61**, 97 (1991)
31. I. Voigt, P. Puhlfürss, J. Töpfer, *Key Engineering Materials* (Trans Tech Publication, Zurich, 1997)
32. L. Sikong, J. Damchan, K. Kooptarnond, S. Niyomwas, Songklanakarin *J. Sci. Technol.* **30**, 385–391 (2008)
33. K. Warriar, S.R. Kumar, C. Sibin, G. Werner, *J. Porous Mater.* **8**, 311 (2001)
34. J.Y.X. Zhao, J. Du, W. Chen, *J. Sol Gel Sci. Technol.* **17**, 163 (2000)
35. M. Hamadani, A. Reisi-vanani, A. Majedi, *J. Iran. Chem. Soc.* **7**, S52–S58 (2010)
36. V. Tajer-Kajinebaf, H. Sarpoolaky, T. Mohammadi, *Int. J. Photoenergy* **2013**, 1–12 (2013)